Battery Materials

International Edition: DOI: 10.1002/anie.201702711
German Edition: DOI: 10.1002/ange.201702711

Transformation of Rusty Stainless-Steel Meshes into Stable, Low-Cost, and Binder-Free Cathodes for High-Performance Potassium-Ion Batteries

*Yun-hai Zhu, Yan-bin Yin, Xu Yang, Tao Sun, Sai Wang, Yin-shan Jiang, Jun-min Yan, and Xin-bo Zhang**

Abstract: *To recycle rusty stainless-steel meshes (RSSM) and meet the urgent requirement of developing high-performance cathodes for potassium-ion batteries (KIB), we demonstrate a new strategy to fabricate flexible binder-free KIB electrodes via transformation of the corrosion layer of RSSM into compact stack-layers of Prussian blue (PB) nanocubes (PB@SSM). When further coated with reduced graphite oxide (RGO) to enhance electric conductivity and structural stability, the low-cost, stable, and binder-free RGO@PB@SSM cathode exhibits excellent electrochemical performances for KIB, including high capacity (96.8 mAh g^{-1}), high discharge voltage (3.3 V), high rate capability (1000 mA g^{-1}; 42 % capacity retention), and outstanding cycle stability (305 cycles; 75.1 % capacity retention).*

The rapid growth of renewable energy resources has created an urgent need to develop a large-scale energy-storage system for grid utilization.[1] Lithium-ion batteries (LIB) are considered as the most promising options for this application, while the use of lithium is impeded by its cost and limited reserves.[2] In response, sodium-ion batteries (SIB) have recently captured considerable attention, because of the abundance of sodium resources and their potential low cost.[3] In fact, the standard potential of K/K^+ couple (−2.92 V versus SHE (standard hydrogen electrode) is much lower than that of Na/Na^+ (−2.71 V vs. SHE) and the natural abundance of potassium is comparably higher than sodium, thus indicating that potassium-ion batteries (KIB) possess a higher energy density and lower cost as compared to SIB. Unfortunately, owing to the larger ionic radius of the K-ion (0.138 nm) compared with the Na-ion (0.102 nm) and the Li-ion (0.076 nm), some promising cathode materials for LIB and SIB are difficult for K-ion insertion/extraction.[4] Hence, development of advanced cathode materials and design of appropriate electrode structures for KIB are urgently desirable but remain a great challenge.

Stainless-steel meshes (SSM) are widely used in screening and filtering under acid or alkali conditions, because of their high filtration accuracy, excellent chemical corrosion resistance, high wear resistance, and high compressive strength. However, owing to the harsh and corrosive working conditions, corrosion cannot be completely avoided. Generally, rusty SSM (RSSM) can be metallurgically reprocessed, which recovers the valuable alloying elements, but has drawbacks including high energy and time costs, and pollution emissions.[5] Thus, it is desirable to develop a low-cost, highly efficient and eco-friendly strategy to recycle the waste RSSM.

Herein, as a proof-of-concept experiment, using RSSM as solid-state iron sources and conductive substrates, we devise a facile method of fabricating flexible binder-free electrodes via transformation of the corrosion layer of RSSM into compact stack layers of Prussian blue (PB) nanocubes (PB@SSM). Moreover, to further enhance conductivity and improve the structural stability of PB@SSM electrodes, a unique reduced graphite oxide (RGO) coated structure has been designed (RGO@PB@SSM). Such a structure not only avoids the agglomeration and detachment of active materials during cycling, but also offers ultrafast electron transportation pathways, leading to high capacity (96.8 mAh g^{-1}), high discharge voltage (3.3 V) and high rate capability (1000 mA g^{-1}; 42 % capacity retention) as well as outstanding cycle stability (305 cycles; 75.1 % capacity retention). To our knowledge, a flexible binder-free KIB electrode in conjunction with such a battery performance has not been reported.

Figure 1 a illustrates the formation of flexible binder-free RGO@PB@SSM-integrated electrodes. Initially, to mimic and expedite the process of natural corrosion, freshly washed SSM is converted into RSSM by a facile hydrothermal treatment in aqueous ammonia solution. Along with this process, the color of SSM changes from silver to brown (insets of Figure S1 a and S2 a, Supporting Information), indicating the successful growth of the rusty layer. As the scanning electron microscopy (SEM) images show, the surface of RSSM is closely packed with irregular particles (Figure 1 b, S2, and S3), which is quite different from the smooth surface of SSM (Figure S1). The thickness of the corrosion layer is approximately 600 nm (Figure S4). Owing to the amorphous characteristics (inset of Figure S3), it cannot be detected by X-ray diffraction (XRD) (Figure 1 e). As the Raman spectra

[*] Y.-h. Zhu, Y.-b. Yin, Dr. X. Yang, T. Sun, S. Wang, Prof. Dr. X.-b. Zhang
State Key Laboratory of Rare Earth Resource Utilization,
Changchun Institute of Applied Chemistry,
Chinese Academy of Sciences
Changchun, 130022 (P.R. China)
E-mail: xbzhang@ciac.ac.cn
Y.-h. Zhu, Y.-b. Yin, S. Wang, Prof. Dr. Y.-S. Jiang, Prof. Dr. J.-M. Yan
Key Laboratory of Automobile Materials (Jilin University), Ministry of Education, Department of Materials Science and Engineering,
Jilin University
Changchun, 130022 (China)
Supporting information and the ORCID identification number(s) for the author(s) of this article can be found under: https://doi.org/10.1002/anie.201702711.

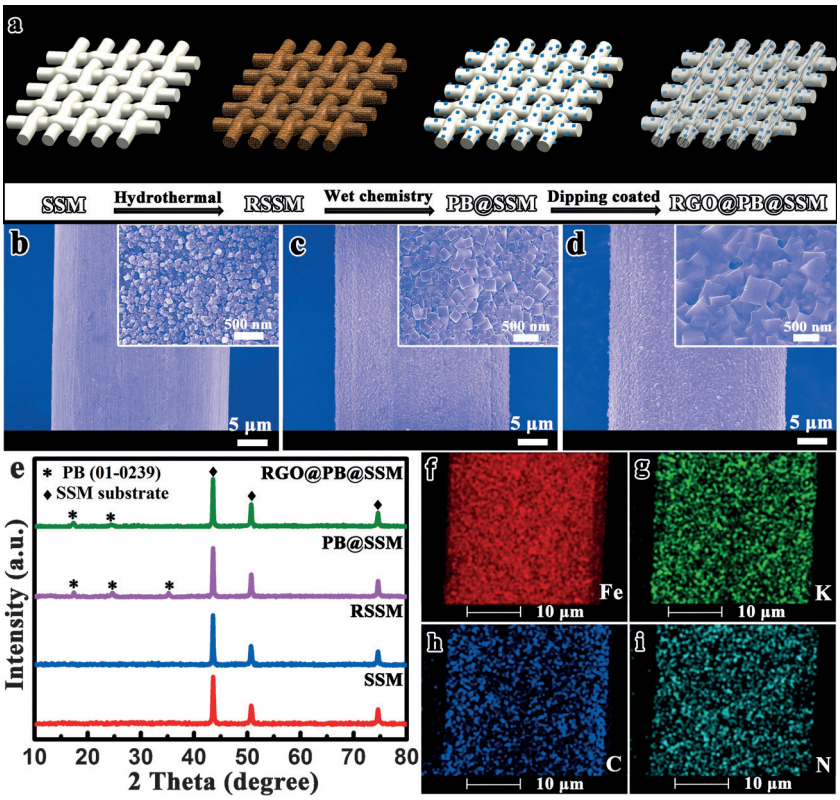

Figure 1. a) Illustration of the formation of flexible binder-free RGO@PB@SSM electrodes. SEM images of RSSM (b), PB@SSM (c), and RGO@PB@SSM (d); inset are the corresponding magnified SEM images. e) XRD spectra of SSM, RSSM, PB@SSM, and RGO@PB@SSM. f–i) EDS mapping of Fe (f), K (g), C (h), and N (i) for RGO@PB@SSM.

(Figure S5) and X-ray photoelectron spectroscopy (XPS) (Figure S6) verified, the uneven particles are mainly composed of Fe (Ni, Cr) oxide/hydroxide.[6] Subsequently, the RSSM is immersed into a potassium ferrocyanide solution containing dilute hydrochloric acid. Accordingly, owing to the acid environment, local dissolution of the metal oxide/hydroxide provides solvated Fe, Ni, and Cr ions, which are immediately consumed by excess ferricyanide ions to form a PB framework at the solid/solution interface. Subsequently, the irregular particles are completely substituted by a compact stack layer (approximately 900 nm, Figure S7) of cubic crystallites (Figure 1c, S8 and S9) accompanied by a simultaneous color change to blue (inset of Figure S8a), thus indicating that PB@SSM electrodes have been assembled successfully. Composition and structural characterization by XRD measurements (Figure 1e) confirm the purity of the final PB product, which is consistent with the Fourier-transform infrared spectroscopy results (Figure S10).[7] It should be noted that there are no identifiable peaks associated with other Prussian blue analogues, possibly due to the low content of Ni and Cr, which is further confirmed by the EDX (energy-dispersive X-ray spectroscopy) spectrum (Figure S11) and inductively coupled plasma-atomic emission spectrometry (ICP-AES) results (Table S1).

For further improvements to the structural stability and conductivity, graphene oxide (GO) is employed to coat the surface of the obtained electrode via a simple dip-coating method, forming GO@PB@SSM. As shown in Figure S12, GO films entirely coat the PB@SSM electrodes, which act as excellent conductive networks to connect the single PB nanocubes. Note that the composition of PB@SSM remains almost unchanged after coating (Figure S15). To further enhance conductivity, GO@PB@SSM electrodes are reduced in potassium borohydride solution to give RGO@PB@SSM. Compared with GO@PB@SSM, the overall structure of the as-prepared electrode remains essentially unchanged (Figure S13a). Magnified SEM images (Figure 1d and S13b) show that RGO films are tightly bound to each nanocube on the obtained electrodes, indicating a robust physical contact. Corresponding EDX elemental mapping (Figure 1f–i) demonstrate that Fe, K, C, and N atoms are homogeneously distributed throughout the electrode. Unexpectedly, the blue color of GO@PB@SSM completely fades after reduction (inset of Figure S13a), while its crystalline structure remains almost unchanged (Figure 1e). It is reasonable to believe that the color change is related to the reduction of Fe^{3+} into Fe^{2+}. For comparison, PB@SSM directly reduced by potassium borohydride was also fabricated (NRPB@SSM), and SEM images (Figure S14) and XRD analyses (Figure S15) confirm that there is no obvious change in its morphology and composition.

Electrical conductivity (EC) of the integrated electrode is crucial for applications in energy storage devices. As shown in Figure 2a, the EC of SSM, RSSM, PB@SSM, NRPB@SSM, GO@PB@SSM, and RGO@PB@SSM electrodes are 1.87×10^5, 1.41×10^5, 1.46×10^5, 1.46×10^5, 1.86×10^5, and $2.23\times10^5\ S\,m^{-1}$, respectively. Note that the EC of RGO@PB@SSM reaches a higher than that of others, even compared to native SSM, thus indicating that the incorporation of RGO significantly improves EC. To investigate the chemical state of the surface of all electrodes, XPS measurements were performed. As shown in Figure 2b, the high resolution Fe $2p_{3/2}$ spectra of all electrodes can be deconvoluted into two types, assigned to $Fe(CN)_6^{4-}$ (approximately 708.7 eV) and $Fe(CN)_6^{3-}$ (approximately 711.3 eV).[8] Interestingly, compared to PB@SSM and GO@PB@SSM, the intensity ratios of $Fe(CN)_6^{4-}$ to $Fe(CN)_6^{3-}$ are higher in NRPB@SSM and RGO@PB@SSM electrodes. Meanwhile, similar results are corroborated by Raman spectra. As shown in Figure 2c and 2d, after reduction, the two peaks located at approximately 2070 and 2015 cm^{-1}, assigned to $Fe(CN)_6^{4-}$, increase in intensity; while the peak located at approximately 2139 cm^{-1}, assigned to $Fe(CN)_6^{3-}$, becomes weaker in intensity.[9] These data could be explained by the reduction of Fe^{3+} into Fe^{2+}. Additionally, two characteristic peaks of graphene at 1350 and 1580 cm^{-1} are identified in the Raman spectra of

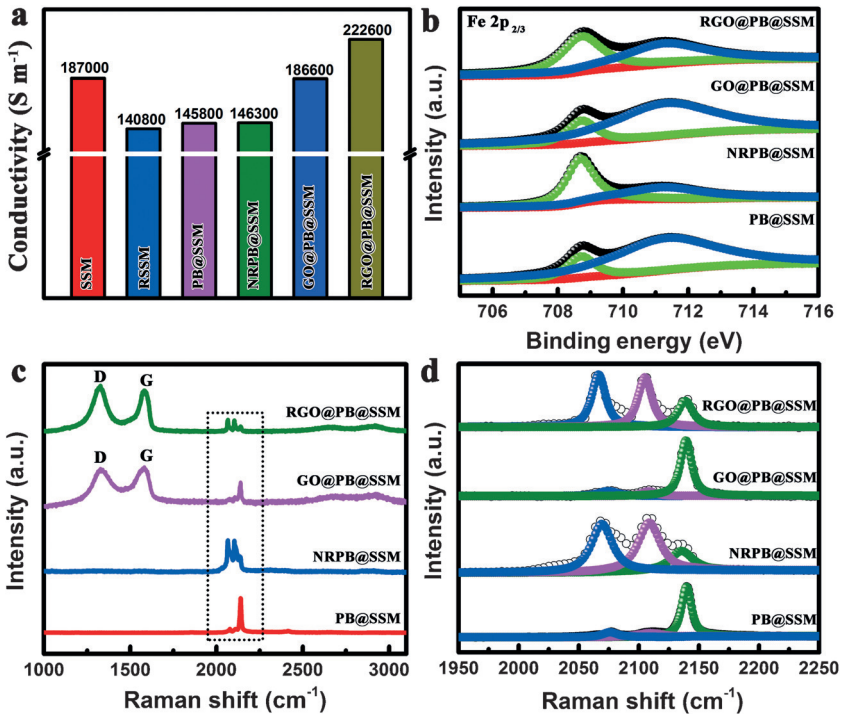

Figure 2. a) Electrical conductivities of SSM, RSSM, PB@SSM, NRPB@SSM, GO@PB@SSM, and RGO@PB@SSM. b) XPS spectra (Fe $2p_{2/3}$) for PB@SSM, NRPB@SSM, GO@PB@SSM, and RGO@PB@SSM. Raman spectra (c) and curve-fitted micro-Raman spectra (d; enlarged view from the dashed box in (c)) for PB@SSM, NRPB@SSM, GO@PB@SSM, and RGO@PB@SSM electrodes.

GO@PB@SSM and RGO@PB@SSM (Figure 2c), which further confirm that GO-coated electrodes have been fabricated successfully. Note that the intensity ratio of the D-band to G-band of GO (I_D/I_G) is higher in RGO@PB@SSM, indicating a reduction in the average size of the sp^2 domains after GO reduction.[10] To further identify the K content in all electrodes, ICP-AES analysis was carried out (Table S1). The result shows the proportions of element K for PB@SSM, NRPB@SSM, GO@PB@SSM, and RGO@PB@SSM are 18.12, 32.49, 17.96, and 30.57 wt%, respectively; confirming that some K ions are introduced into the framework of PB during reduction. Coin cells with metallic K counter-electrodes are assembled and the galvanostatic discharge/charge technique is employed to evaluate the electrochemical performance of all electrodes. As shown in Figure 3a–c, the initial charge capacities of PB@SSM, NRPB@SSM and RGO@PB@SSM are 15.7, 118.7 and 117.3 mAh g^{-1}, respectively, and their initial discharge capacities are 79.0, 90.2 and 96.8 mAh g^{-1}, respectively (the capacity of SSM is negligible, Figure S16). It should be noted that the NRPB@SSM and RGO@PB@SSM electrodes show much higher initial charge capacities compared with PB@SSM due to relatively high contents of K for NRPB@SSM and RGO@PB@SSM. Note that high K concentration in the initial PB framework is available for a non-potassium metal anode to make practical K-ion full batteries.[11] Importantly, the discharge capacity of RGO@PB@SSM stays nearly unchanged, and the overlapping voltage profiles in Figure 3c demonstrate their excellent electrochemical reversibility. In contrast, the discharge capacities of PB@SSM and NRPB@SSM decline gradually over the first five cycles.

To further analyze electrochemical behavior, differential analyses are employed. As shown in Figure 3a–c (insets), all the electrodes exhibit one pair of redox peaks located at approximately 3.5 V on charge and approximately 3.3 V on discharge, which corresponds to the redox couple of the carbon-coordinated Fe^{III}/Fe^{II}.[12] Note that the potential interval between the anodic and cathodic peaks of RGO@PB@SSM electrode is only 0.13 V, much lower than those of PB@SSM (0.25 V) and NRPB@SSM electrodes (0.23 V). Moreover, the redox peak profile of RGO@PB@SSM electrodes is more symmetric and sharper than that of the other electrodes, indicating that the redox kinetics are enhanced due to the

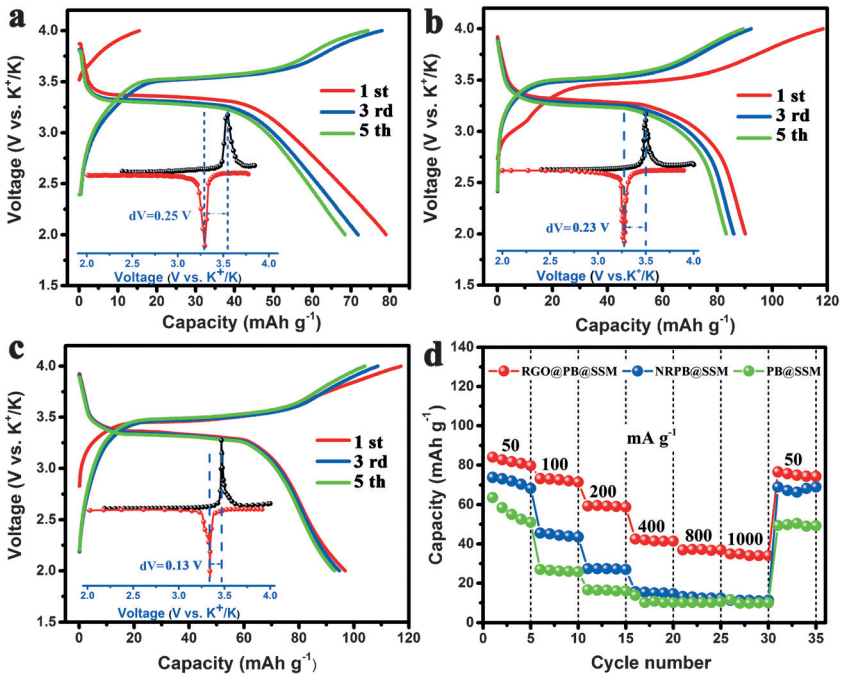

Figure 3. Galvanostatic charge and discharge curves of PB@SSM (a), NRPB@SSM (b), and RGO@PB@SSM (c) at a current of 10 mA g^{-1}; insets are the corresponding differential galvanostatic (dQ/dV) profiles during the third cycle. d) Rate capabilities of PB@SSM, NRPB@SSM and RGO@PB@SSM electrodes.

improved conductivity. It should be noted that all flexible binder-free electrodes deliver superior electrochemical performances compared with traditional electrodes (PB as active material mixed with binder and conductive carbon, Figure S17). Another noteworthy feature of the RGO@PB@SSM electrode is the rate capability. As shown in Figure 3d, the RGO@PB@SSM electrode can deliver discharge capacities of 84, 60 and 43 mA h g^{-1} at a current densities of 50, 200 and 400 mA g^{-1}, respectively. Unexpectedly, even at a very high current density of 1000 mA g^{-1}, the discharge capacity can still reach 35 mA h g^{-1}, corresponding to 42% of its initial reversible capacity. In sharp contrast, NRPB@SSM and PB@SSM electrodes exhibit much lower capacities of 11.28 and 10.01 mA h g^{-1}, respectively, both at a current density of 1000 mA g^{-1}, and thus only achieving 15.3 and 15.7% of their original capacities.

Inspired by the excellent rate capability of RGO@PB@SSM, we then test the cycling stability under high discharge/charge current densities. As shown in Figure 4a, the RGO@PB@SSM electrodes exhibit stable capacities of 61.4, 52.1, and 46.6 mAh g^{-1} at current densities of 50, 100, and 200 mA g^{-1}, respectively, even after 305 cycles. These correspond to 75.1, 71.8, 71.6% of their initial reversible capacities. Importantly, the charge and discharge behaviors of the RGO@PB@SSM electrodes remained almost unchanged even under the high current density of 200 mA g^{-1} (Figure S18). In contrast, the cycle performances of PB@SSM and NRPB@SSM electrodes are inferior (Figure S19 and S20); only 45.1 and 46.9% of their original capacities can be preserved after 300 cycles. To further investigate the structural changes upon cycling, we performed SEM measurements for all electrodes after 50 cycles. As shown in Figure S21, the RGO@PB@SSM electrode protected by graphene layers is preserved without obvious structural damage. Moreover, graphene layers absorb well on the surface of SSM, revealing that the obtained coated structure is robust enough to withstand repeated K^+ insertion/extraction. In contrast, other electrodes suffer from serious structural damage and exfoliation of active materials, likely responsible for capacity decreases upon cycling. Electrochemical impedance spectroscopy is employed to further understand the enhanced electrochemical performance of the RGO@PB@SSM electrodes. As shown in Figure 4b, all of the Nyquist plots are composed of a depressed semicircle in the high-frequency region (corresponding with the charge transfer resistance (*R*ct)), and a sloped line in the low frequency region (owing to the Warburg resistance (*W*) related to the K^+ ion diffusion in PB).[13] Quantitatively, based on the fitted equivalent circuit, the *R*ct of RGO@PB@SSM is calculated to be around 3600 Ω, while those for NRPB@SSM (8800 Ω), and PB@SSM (9490 Ω) are much higher, indicating that RGO@PB@SSM electrodes show improved electron and ion transport. As for the RGO@PB@SSM electrodes, the significantly improved electrochemical performance might be related to the unique RGO-coated structure and high conductivity. As shown in Figure 4c, the generated PB nanocubes in the interlayer between the RGO film and SMM substrate show a close and robust physical contact with highly conductive SSM substrate and RGO, enabling ultrafast electron transport and avoiding the agglomeration and detachment of PB nanocubes. Additionally, the open framework of PB allows for rapid K^+ ion transport. Based on the unique structure design and selection of appropriate materials, we present the first high-performance, flexible, binder-free KIB cathode (Table S2). Thus our electrodes have enormous potential for applications in flexible electronic devices.

In summary, to convert waste materials into commodity products, we developed a facile strategy to fabricate flexible binder-free KIB electrodes from RSSM. When combined with a unique RGO-coated structure, the as-prepared RGO@PB@SSM electrodes exhibit excellent electrochemical characteristics for KIB, including high capacity (96.8 mAh g^{-1}), high discharge voltage (3.3 V), high rate capability (1000 mA g^{-1}; 42% capacity retention), as well as outstanding cycle stability (305 cycles; 75.1% capacity retention). The proposed method opens new avenues for the reuse of rusty stainless steel toward new value-added applications, which are of great importance to assist the efforts to build a resource-sustainable and environmentally friendly society.

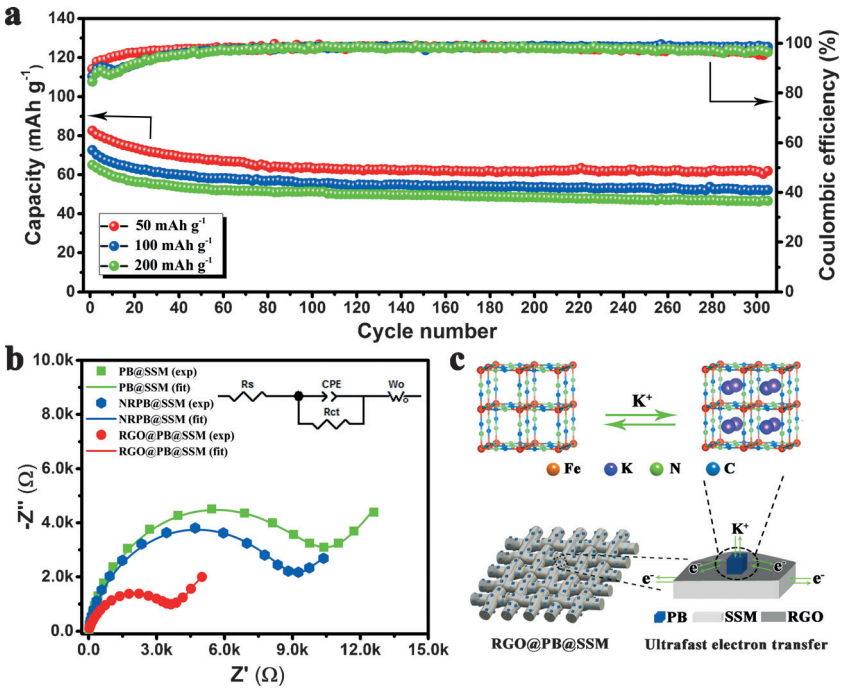

Figure 4. a) Cycling performance of RGO@PB@SSM electrodes under different current densities. b) Nyquist plots of PB@SSM, NRPB@SSM and RGO@PB@SSM electrodes. c) Potassium transport processes for RGO@PB@SSM electrodes.

Acknowledgements

This work is financially supported by National Natural Science Foundation of China (51522101, 51471075, 51631004, and 51401084).

Conflict of interest

The authors declare no conflict of interest.

Keywords: binder-free electrodes · graphene oxide · potassium-ion batteries · rusty stainless steel meshes

How to cite: *Angew. Chem. Int. Ed.* **2017**, *56*, 7881 –7885
Angew. Chem. **2017**, *129*, 7989 –7993

[1] a) B. Kang, G. Ceder, *Nature* **2009**, *458*, 190; b) B. Dunn, H. Kamath, J. M. Tarascon, *Science* **2011**, *334*, 928; c) C. D. Wessells, R. A. Huggins, Y. Cui, *Nat. Commun.* **2011**, *2*, 550.

[2] a) C. Zu, H. Li, *Energy Environ. Sci.* **2011**, *4*, 2614; b) S. W. Kim, D. H. Seo, X. Ma, G. Ceder, K. Kang, *Adv. Energy Mater.* **2012**, *2*, 710; c) Y. Fang, L. Xiao, X. Ai, Y. Cao, H. Yang, *Adv. Mater.* **2015**, *27*, 5895.

[3] a) X. Xiang, K. Zhang, J. Chen, *Adv. Mater.* **2015**, *27*, 5343; b) S. Yuan, Y. Liu, D. Xu, D. Ma, S. Wang, X. Yang, Z. Cao, X. Zhang, *Adv. Sci.* **2015**, *2*, 1400018; c) T. Sun, Z. Li, H. Wang, D. Bao, F. Meng, X. Zhang, *Angew. Chem. Int. Ed.* **2016**, *55*, 10662; *Angew. Chem.* **2016**, *128*, 10820.

[4] Z. Jian, Z. Xing, C. Bommier, Z. Li, X. Ji, *Adv. Energy Mater.* **2016**, *6*, 1501874.

[5] a) B. K. Reck, M. Chambon, S. Hashimoto, T. E. Graedel, *Environ. Sci. Technol.* **2010**, *44*, 3940; b) X. Zhang, X. Hong, *Resour. Conserv. Recycl.* **2011**, *55*, 745.

[6] a) D. L. A. de Faria, S. Venâncio Silva, M. T. de Oliveira, *J. Raman Spectrosc.* **1997**, *28*, 873; b) J. Ma, J. Lian, X. Duan, X. Liu, W. Zheng, *J. Phys. Chem. C* **2010**, *114*, 10671; c) R. D. Smith, M. S. Prevot, R. D. Fagan, S. Trudel, C. P. Berlinguette, *J. Am. Chem. Soc.* **2013**, *135*, 11580.

[7] a) P. J. Kulesza, M. A. Malik, A. Denca, J. Strojek, *Anal. Chem.* **1996**, *68*, 2442; b) P. Nie, L. Shen, G. Pang, Y. Zhu, G. Xu, Y. Qing, H. Dou, X. Zhang, *J. Mater. Chem. A* **2015**, *3*, 16590.

[8] a) T. Yamashita, P. Hayes, *Appl. Surf. Sci.* **2008**, *254*, 2441; b) L. Cao, Y. Liu, B. Zhang, L. Lu, *ACS Appl. Mater. Interfaces* **2010**, *2*, 2339.

[9] a) D. Yang, J. Xu, X. Z. Liao, H. Wang, Y. S. He, Z. F. Ma, *Chem. Commun.* **2015**, *51*, 8181; b) D. Yang, L. Han, Y. Yang, L.-B. Zhao, C. Zong, Y.-F. Huang, D. Zhan, Z.-Q. Tian, *Angew. Chem. Int. Ed.* **2011**, *50*, 8679; *Angew. Chem.* **2011**, *123*, 8838.

[10] a) S. Stankovich, D. A. Dikin, R. D. Piner, K. A. Kohlhaas, A. Kleinhammes, Y. Y. Jia, Y. Wu, S. T. Nguyen, R. S. Ruoff, *Carbon* **2007**, *45*, 1558; b) B. Qu, C. Ma, G. Ji, C. Xu, J. Xu, Y. S. Meng, T. Wang, J. Y. Lee, *Adv. Mater.* **2014**, *26*, 3854.

[11] L. Wang, J. Song, R. Qiao, L. A. Wray, M. A. Hossain, Y. De Chuang, W. Yang, Y. Lu, D. Evans, J. J. Lee, S. Vail, X. Zhao, M. Nishijima, S. Kakimoto, J. B. Goodenough, *J. Am. Chem. Soc.* **2015**, *137*, 2548.

[12] a) C. Zhang, Y. Xu, M. Zhou, L. Liang, H. Dong, M. Wu, Y. Yang, Y. Lei, *Adv. Funct. Mater.* **2017**, *27*, 1604307; b) Y.-h. Zhu, S. Yuan, D. Bao, Y.-b. Yin, H.-x. Zhong, X.-b. Zhang, J.-m. Yan, Q. Jiang, *Adv. Mater.* **2017**, *29*, 1603719.

[13] a) Y. Jiang, Z. Z. Yang, W. H. Li, L. C. Zeng, F. S. Pan, M. Wang, X. Wei, G. T. Hu, L. Gu, Y. Yu, *Adv. Energy Mater.* **2015**, *5*, 1402104; b) S. Yuan, Y. Zhu, W. Li, S. Wang, D. Xu, L. Li, Y. Zhang, X. Zhang, *Adv. Mater.* **2017**, *29*, 1602469.

Manuscript received: March 15, 2017
Accepted manuscript online: May 3, 2017
Version of record online: June 5, 2017

